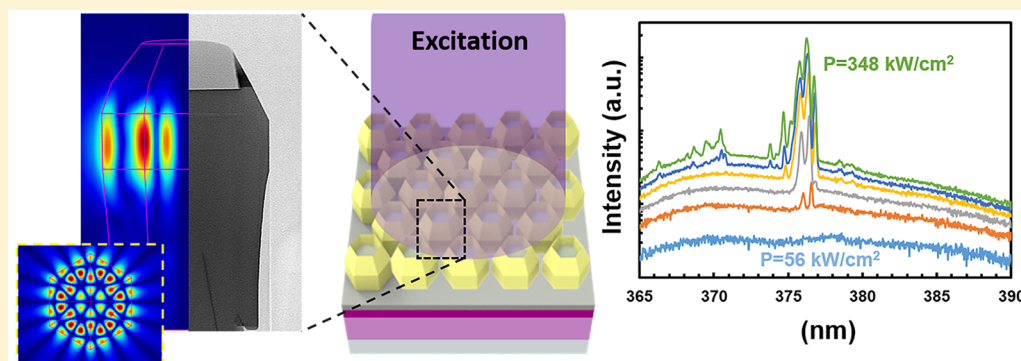


Collective Lasing Behavior of Monolithic GaN–InGaN Core–Shell Nanorod Lattice under Room Temperature

Chia-Yen Huang,*¹ Jing-Jie Lin, Tsu-Chi Chang, Che-Yu Liu, Tzu-Ying Tai, Kuo-Bin Hong, Tien-Chang Lu, and Hao-Chung Kuo

Department of Photonics and Institute of Electro-Optical Engineering, National Chiao Tung University, 1001 Ta Hsueh Road, Hsinchu 300, Taiwan

S Supporting Information



ABSTRACT: We demonstrated a monolithic GaN–InGaN core–shell nanorod lattice lasing under room temperature. The threshold pumping density was as low as 140 kW/cm^2 with a quality factor as high as 1940. The narrow mode spacing between lasing peaks suggested a strong coupling between adjacent whisper gallery modes (WGM), which was confirmed with the far-field patterns. Excitation area dependent photoluminescence revealed that the long-wavelength lasing modes dominated the collective lasing behavior under a large excitation area. The excitation-area-dependent lasing behavior resulted from the prominent optical coupling among rods. According to the optical mode simulations and truncated-rod experiments, we confirmed that the fine-splitting of lasing peaks originated from the coupled supermodes existing in the periodic nanorod lattices. With wavelength-tunable active materials and a wafer-level scalable processing, patterning optically coupled GaN–InGaN core–shell nanorods is a highly practical approach for building various on-chip optical components including emitters and coupled resonator waveguides in visible and ultraviolet spectral range.

KEYWORDS: Core–shell, InGaN, whisper gallery modes, supermodes, monolithic, collective lasing

Nitride-based laser is an ideal light source for many applications ranging from optical storage, color display, illumination, and other industrial uses because of its short wavelengths and high robustness. Conventional Fabry–Pérot (FP) type edge-emitting lasers and vertical-cavity surface-emitting lasers (VCSELs) have been demonstrated with continuous-wave operation under room temperatures in various platforms.^{1–4} Nitride-based microcavity lasers were also a great research interest for their low threshold pumping density and high speed, which are essential for pushing photonic chips toward the visible and ultraviolet spectral range. Nanolasers in FP type have been demonstrated with pure GaN nanowires or InGaN–GaN core–shell rods.^{5–8} However, their fabrication and manipulation involved heterogeneous catalytic synthesis or delicate optomechanical processes, which brought significant challenges for large-area fabrication and device integration. Therefore, high quality factor (Q) microcavity lasers with higher feasibility for monolithic fabrication were also intensively studied; for example, whisper gallery mode (WGM) lasers.

Suspended microdisk with multiple-quantum-well (MQW) structure was a suitable cavity for high- Q WGM lasers.^{9–11} However, the reported diameter of these microdisks were limited to a few micrometers to tens of micrometers to suppress the scattering loss and guiding loss through the evanescent field, especially when the cavity was formed by top-down etching processes. Cavities with atomically flat crystallographic planes formed by bottom-up regrowth processes might be the solution for submicron WGM cavities with a decent Q factor. Furthermore, the improved active materials quality by lateral epitaxial regrowth and a polarized emission from nonpolar MQWs all favored lasing action in InGaN–GaN core–shell structures.^{12,13} To date, electroluminescence¹⁴ and FP-type optically pumped lasing have been reported⁶ but there is no observation of WGM lasing in this structure yet. Chang et

Received: July 10, 2017

Revised: September 2, 2017

Published: September 19, 2017

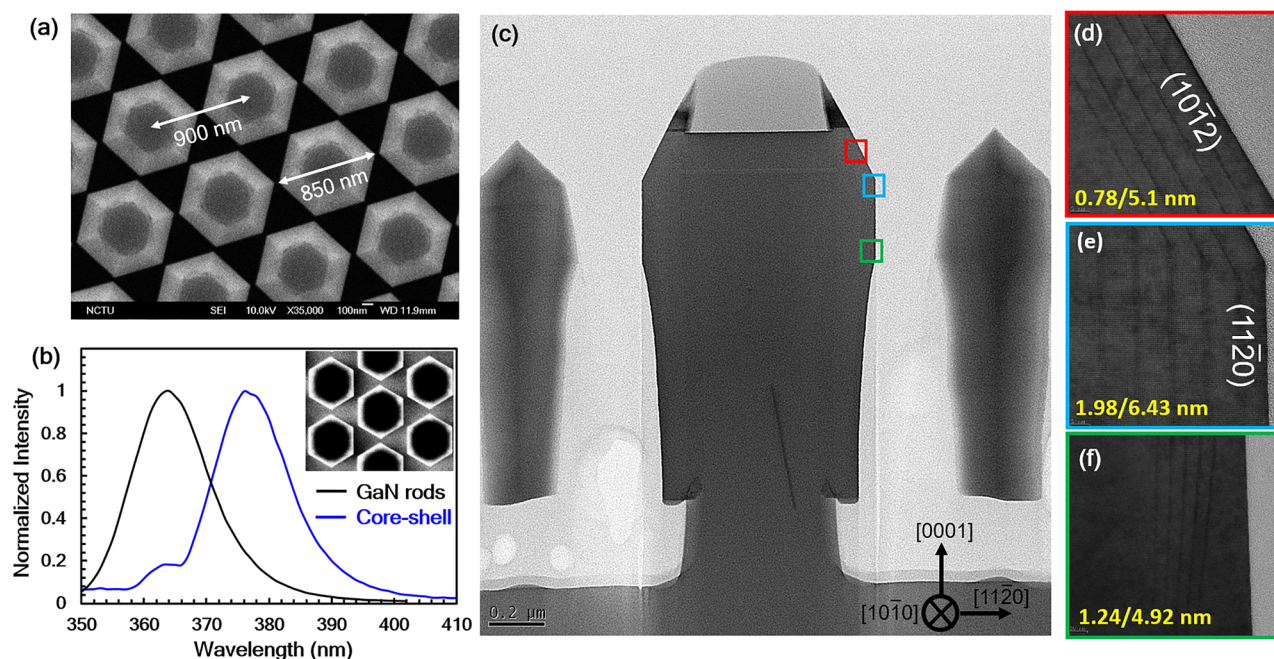


Figure 1. (a) SEM top-view image of core-shell nanorod array after regrowth. (b) CL spectrum of GaN rods before regrowth (black) and core-shell structure (blue). Inset is the panchromatic CL image of full core-shell structure. (c) Cross-sectional TEM images of the core-shell structure with higher magnification near the (d) semipolar facets and (e) upper part and (f) lower part of nonpolar facets. Average QW/barrier thicknesses in each figure were noted in yellow.

al. once demonstrated random lasing with quasicrystal rod arrays with similar core-shell structures to those in ref 15.¹⁶ However, the threshold pumping densities were as high as 2.5 MW/cm² to 6 MW/cm². In this report, we demonstrated room-temperature lasing of a monolithic GaN-InGaN core-shell nanorod lattice. The threshold pumping density (P_{th}) was as low as 140 kW/cm² under room temperature with lasing peak wavelengths around 376 nm. Mode-coupling and splitting phenomena due to the vicinity of rods were also discussed.

Hexagonal nanorod lattice was fabricated on GaN-on-sapphire templates. The hexagonal core-shell structure was achieved by n-GaN and MQW regrowth in metal organic chemical vapor deposition (MOCVD). According to previous studies, direct regrowth on nanorods resulted in nonuniform wavelength distribution and irregular shapes of cavity.^{15,16} For example, the threshold pumping densities in ref 16 were nearly 20 times higher than our reported value. Such high threshold pumping density was partly attributed to the high In homogeneity within the rod. Strong In segregation was observed in rod tips and corners, resulting in a high internal loss due to parasitic bandedge absorption. In this study, a series of passivation steps were performed to limit the regrowth only on the sidewalls to improve the homogeneity (see Supporting Information). Figure 1a was a scanning electron microscope (SEM) image from the top-view of the core-shell nanorod lattice. Crystallographic hexagons were aligned periodically in a 6-fold symmetry. The cathodoluminescence (CL) spectrum before and after MOCVD regrowth was plotted in Figure 1b. The emerging 375 nm CL signal after regrowth confirmed that InGaN QWs in shell have significant contribution in vicinal lasing peaks. Because the GaN in the core region was passivated by SiN_x hardmask, the uncovered InGaN QWs had a stronger contribution in the integrated CL spectrum. In PL measurements, the emission intensities from GaN and InGaN QWs were in the similar level because the

dielectrics were transparent to excitation sources. According to the transmission electron microscopy (TEM) images in Figure 1c, few indium clusters at the edges of semipolar (10 $\bar{1}2$) planes were still observed, but the amount was much less significant than those in ref 15. The rod width was largest in the top 200 nm and eventually shrank toward the field due to the precursor consumption during regrowth, which fortunately provided a decent out-of-plane optical confinement. The In composition of the quantum wells estimated by energy dispersion spectroscopy was around 3% ~ 4%, whose bandgap was consistent with the CL spectrum. The In composition in the lower part of the quantum wells was a bit higher than the average value, and the well thicknesses were also lower (see Supporting Information). As a result, the wavelength redshift due to a higher In composition was compensated by the blueshift due to a thinner quantum well. The CL spectrum still appeared to be narrow without tails or shoulder in long wavelength side.

The 355 nm Nd:YVO₄ pulse laser under room temperature was used for excitation. In the angle-resolved PL (AR-PL) measurement, the laser incident angle was 45° from the sample normal and the PL was collected by optical fiber mounted on a rotatable mechanic arm centering on the sample. For the rest of power-dependent PL measurement, both excitation and collection were fixed along the normal direction of the sample for a better estimation of excitation area. The laser beam was focused by 100 times magnification objective lens with NA = 0.55. The excitation power was controlled by attenuation plates in front of the excitation source. The laser spot size was evaluated by comparing the CCD image of laser spot illuminating on the reference sample with distance markers. AR-PL measurements were performed between principle crystal orientations: *c*-axis to *m*-axis (*c*-to-*m* scan), and *c*-axis to *a*-axis (*c*-to-*a* scan), as illustrated in Figure 2a. The intensity mapping before and after lasing were shown in Figure 2b–e. *c*,

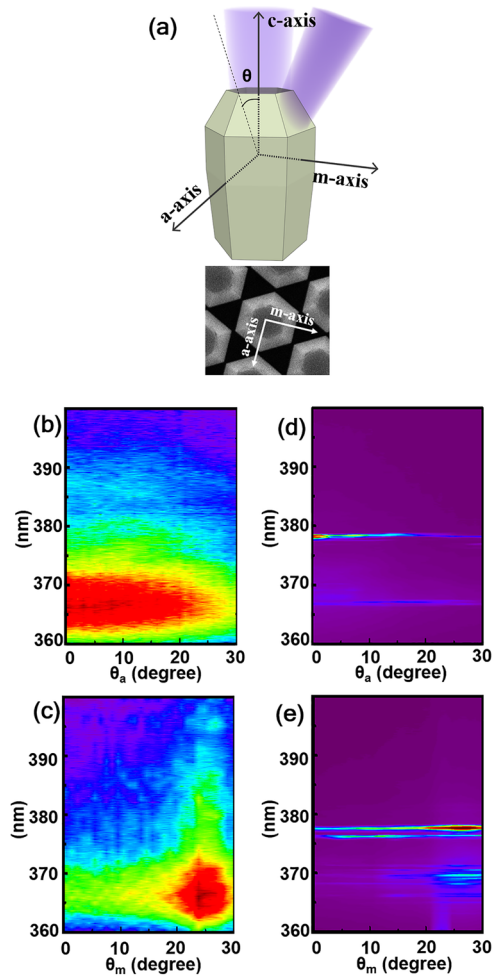


Figure 2. (a) Notation of AR-PL measurement in a three-dimensional illustration and in a top-view SEM image. θ is the inclination angle between the emission direction and the normal axis of rods. (b–e) AR-PL intensity mapping of spontaneous emission spectrum and lasing spectrum in the c -to- a scan (b,d) and c -to- m scan (c,e), respectively.

m -, and a -axis represented the $[0001]$, $[10\bar{1}0]$, and $[11\bar{2}0]$ direction in wurtzite structure, respectively. θ_a was the inclination angle between the emitting direction and the c -axis in the c -to- a scan, and the same nomenclature applied to θ_m . The spontaneous emission was strongest in the normal direction in the c -to- a scan and $\theta_m \sim 25^\circ$ in the c -to- m scan. The lasing spectrum was also strongest along $\theta_a = 0^\circ$ in the c -to- a scan, and $\theta_m \sim 29^\circ$ in c -to- m scan. Although the standing nanorods were aligned periodically, neither wavelength-dependent Fabry–Pérot fringes nor angle-dependent photonic crystal fringes were observed. This indicated the lasing modes shall be highly in-plane, and the interaction among rods mostly happened within a short-range. Long-range photonic-crystal-like lasing shall not play an important role in this study.

Three-dimensional (3D) mode simulations were conducted by COMSOL Multiphysics to study the mode profile and its relevance to far field patterns. The geometry parameters in simulations followed SEM and TEM measurements and the refractive indices for GaN and InGaN were set to be 2.56 and 2.62, respectively. Figure 3a–c shows two strong candidates for the lasing action. Both modes possessed an in-plane high-order WGM in the hexagon cross section (Figure 3c) while the

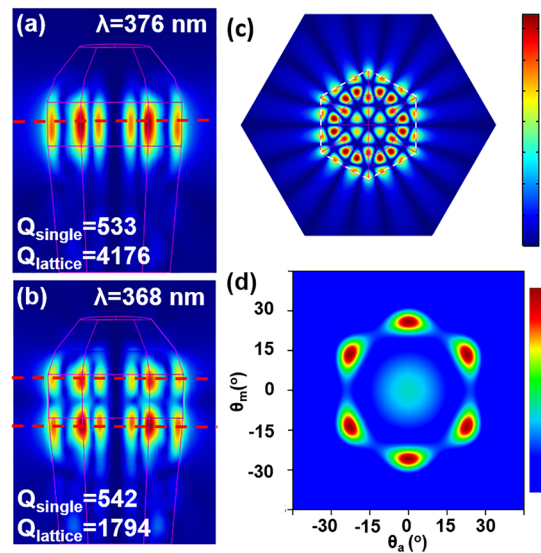


Figure 3. Simulated intensity profile of (a) 376 nm and (b) 368 nm lasing mode along the normal direction. Red dashed line marked the planes with local maximum intensity. (c) The in-plane intensity profile along the red dashed lines. Since the profiles were very close, only one of them was presented. (d) The far-field pattern of the 376 nm mode with a reflective interface below the rod.

longitudinal mode along the c -axis could be either in fundamental mode (Figure 3a) or in second order mode (Figure 3b). The resonant wavelength for the fundamental and second-order longitudinal modes was 376 and 368 nm, respectively, which is close to the experimental data. According to the CL, the cavity modes near 376 nm better matched the peak of InGaN QWs' gain spectrum. Although the GaN in the core region might also contribute the gain, we named the modes close to 376 nm as “InGaN modes” for brevity concern in this report. Similarly, modes located between 368 to 371 nm were named as “GaN modes-1”, and the rest of peaks below 367 nm were named as “GaN modes-2”. The simulated far-field pattern of the 376 nm mode considering backside reflection were shown in Figure 3d. The maximum intensity occurred at $\theta_m = 28^\circ$, which is in good agreement with the Figure 2e. The local maximum at $\theta_{a/m} = 0^\circ$ was attributed to the backside scattering from the bottom. The good agreement between optical simulations and experimental data further confirmed the type of lasing mode in the periodical rod lattice.

Power-dependent PL were also conducted under room temperature. The excitation and detection were fixed along the normal direction with a relatively large spot size (in diameter, $D \sim 120 \mu\text{m}$) first. Power-dependent PL spectrum and light-in, light-out, full width at half-maximum (L–L–fwhm) curves were plotted in Figure 4a,b. Two lasing peaks ($\lambda_{\text{peak}} = 375.9$ and 376.4 nm) first emerged under $P = 116 \text{ kW}/\text{cm}^2$ and the number of peaks increased as P increased. The fwhm of the strongest peak was 0.22 nm, yielding a quality factor of 1940. Assuming a 100% absorption of excitation source by active materials, the upper bound of extracted threshold pumping density (P_{th}) was $140 \text{ kW}/\text{cm}^2$ from the L–L–fwhm curve. The degree of polarization (DOP) was also measured along normal direction beneath and above P_{th} . DOP was estimated by following equation

$$\text{DOP} = \frac{I_{\text{max}} - I_{\text{min}}}{I_{\text{max}} + I_{\text{min}}}$$

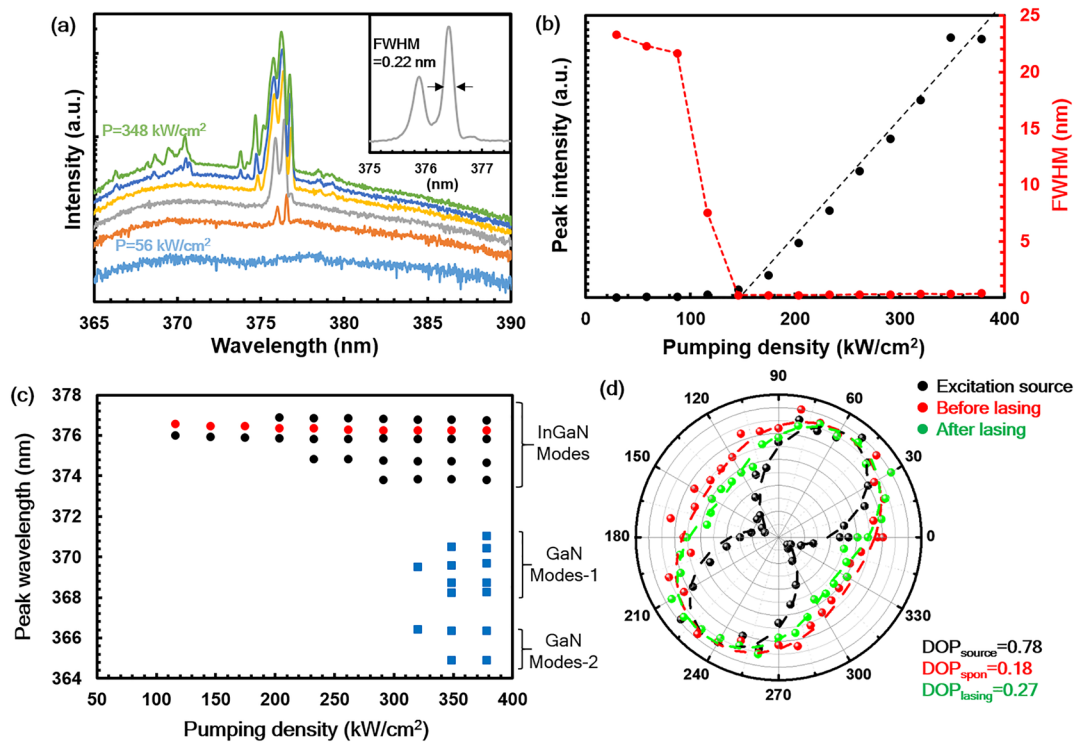


Figure 4. (a) Power-dependent PL spectrum of rod array in logarithm scale. Inset is the PL spectrum near the lasing peak under $P = 174 \text{ kW/cm}^2$ in linear scale. (b) L-L-fwhm curves extracted from (a). (c) Power-dependent peak distribution extracted from (a). The strongest peak was marked in red. (d) Degree of polarization measurement of excitation source (black); InGaN emission before (red) and after (green) lasing.

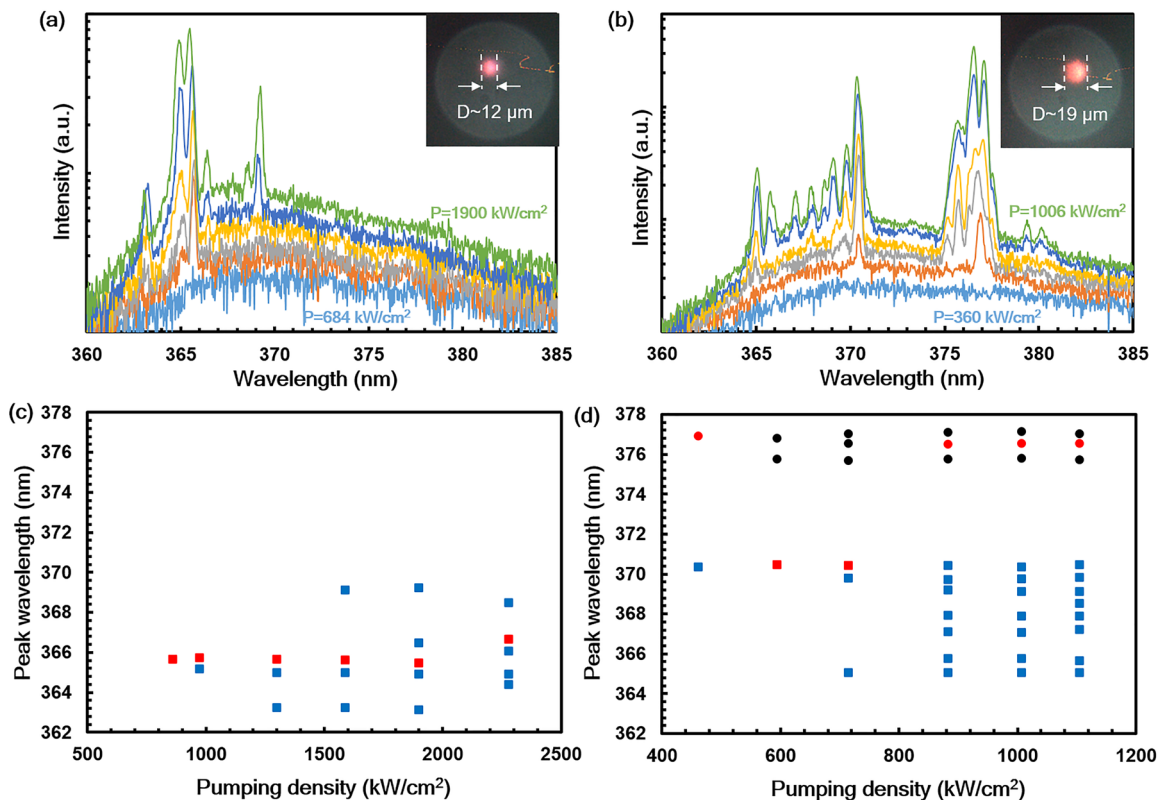


Figure 5. Power-dependent PL spectrum of rod array in logarithm scale with the diameter (D) of excitation area (a) $D = 12 \mu\text{m}$ and (b) $D = 19 \mu\text{m}$. The insets are the CCD image of the laser spot. (c,d) Power-dependent peak distribution extracted from (a,b), respectively.

where I_{max} and I_{min} were the maximum and minimum intensities detected with the rotational polarizer. DOP of

InGaN emission before and after lasing were 0.18 and 0.27, respectively, while the strongest polarization was parallel to the

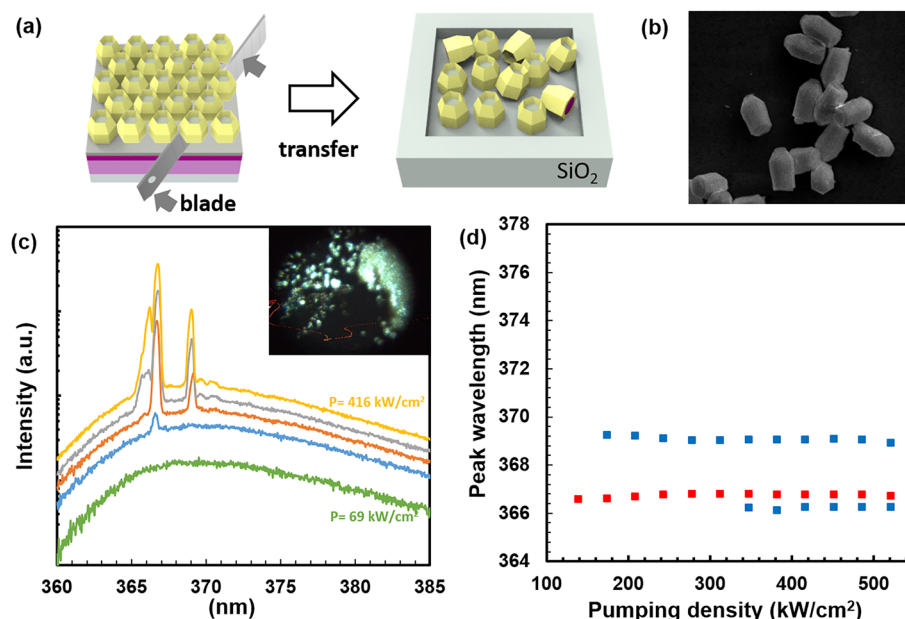


Figure 6. (a) Schematic processing flow of rod transferring from the original template to a foreign SiO_2 substrate by blade. (b) SEM image of transferred rods on SiO_2 . (c) Power-dependent PL spectrum of truncated rods in logarithm scale. Inset is a CCD image of transferred rods illuminated by mercury lamp. Rods were glowing in light-green. (d) Power-dependent peak distribution extracted from (c). The strongest peak was marked in red.

excitation source. Therefore, the actual DOP shall be lower than these values. Such low DOPs after lasing also supported a highly in-plane cavity mode. The lasing peak wavelength along with pumping power density were summarized in Figure 3c. The first two peaks emerged around 376 nm at low P , and vicinal peaks emerged as P increased. Under $P = 196 \text{ kW/cm}^2$, five discernible peaks were observed between 373 to 377 nm. The peaks spacing ranged from 0.4 to 1 nm, which was too small to be different orders of WGM.¹⁷ The fine splitting in either InGaN modes or GaN modes might be attributed to the following two reasons: (1) the size or composition inhomogeneity of excited rods resulted in a distribution of lasing peaks, and some of them just lased under a relatively low pumping density. (2) The formation of “supermodes” by the optical coupling between adjacent high Q resonators, which was also experimentally observed in coupled semiconductor lasers in other materials system.^{18–20}

To clarify the origin of peak multiplication, we conducted similar PL measurements with a smaller excitation area. ($D = 12$ and $19 \mu\text{m}$). The power-dependent PL spectrum and peak distribution were plotted in Figure 5. If the multiple peak originated from the local size or composition fluctuation, reducing the excitation area shall reduce the number of lasing peaks significantly because of a much less number or excited rod. For example, the number of excited rod with $D = 19 \mu\text{m}$ is only 2.5% of that with $D = 120 \mu\text{m}$. However, the number of peaks (N_{peak}) under high excitation is 11, which was close to that with $D = 120 \mu\text{m}$ ($N_{\text{peak}} = 12$). For $D = 12 \mu\text{m}$, the maximum N_{peak} seems to be reduced, but it is attributed to the absence of InGaN mode lasing. Therefore, the peak multiplication under high excitation is not likely due to the local size/composition inhomogeneity. The composition or size distribution only caused the lasing wavelength and threshold pumping density fluctuation through the wafer. However, the trend of collective lasing behavior was found consistent: under a large excitation area, the dominant lasing modes were InGaN

modes. As the excitation area reduced, the dominance gradually shifted from InGaN modes to GaN modes. In Figure 5d, InGaN modes and GaN modes appeared under similar excitation level and their relative intensities were also comparable. If the excitation area was further reduced, only GaN-modes could be observed before the material were degraded due to over excitation. We attributed these collective lasing behaviors by the stronger rod-to-rod coupling for InGaN modes rather than GaN modes, which was further verified by PL experiments on truncated rods.

To further confirm the asymmetry of rod-to-rod coupling among different modes, we mechanically removed many rods from the template by blades and transferred them to a SiO_2 substrate as depicted in Figure 6a,b. Because these truncated rods were arbitrarily attached on the surface, the probability of forming closely coupled rods became much lower. Therefore, the peak-splitting phenomena was expected to be suppressed. These truncated rods were illuminated under a large excitation area ($D \sim 100 \mu\text{m}$) to excite as much rods as possible. Two peaks emerged first after lasing, and the third peak appeared when P exceeded 346 kW/cm^2 . The N_{peak} remained at 3 before rods were burnt. Therefore, the excess of N_{peak} in Figures 4c and 5c,d could only be attributed to lasing modes which only existed in the monolithic lattice. This is the direct evidence of the supermode lasing in the nanorod lattice. Summing up all the PL experiments, following conclusions could be drawn: (1) Limited lasing modes existed in a single nanorod. The multiplication of peaks in the monolithic lattice was a result of rod-to-rod mode interactions. (2) The GaN-modes prevailed in a single rod but the dominant mode could switch from GaN modes to InGaN modes as the extent of lasing rods increased in the system.

In the mode simulations of Figure 3a,b, the quality factor of single rod (Q_{single}) for the InGaN modes and GaN modes were 533 and 542, respectively. However, if we properly set the periodic boundary condition to simulate the infinite in-plane

lattice, the quality factor (Q_{lattice}) for InGaN mode and GaN mode increased to 4176 and 1794, respectively. In an optical waveguide, the penetration depth (d_p) of the evanescent field is given as²¹

$$d_p = \frac{\lambda}{4\pi\sqrt{n^2(\lambda)\sin^2\theta - 1}}$$

where λ is the resonant free space wavelength, $n(\lambda)$ is the wave-dependent phase index, and θ is the incident angle of light within the waveguide. Since the InGaN modes have a longer wavelength and smaller refractive index,^{22,23} its penetration depth was longer than that of GaN modes. Besides, the nature of fundamental mode also favored the rod-to-rod or rod-to-substrate interactions because its maximum intensity was surrounded by vertical facets. Therefore, the InGaN modes penetrate into adjacent microcavities or interfaces more effectively. Optical simulation in Figure 7a showed the mode

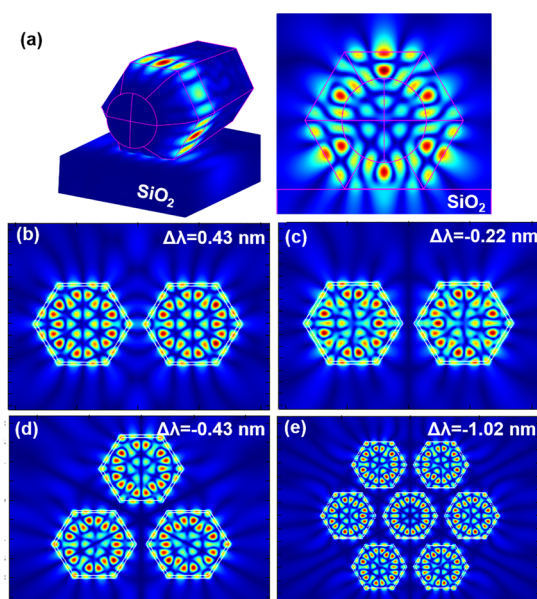


Figure 7. (a) Mode profiles of a truncated rod horizontally lying on the SiO_2 substrate. Two-dimensional supermode intensity profile incorporating (b,c) two rods, (d) three rods, and (e) seven rods. All rod-to-rod spacing was set 50 nm.

profile of rods horizontally lying on the substrate. Photons were leaked into substrate so the Q factor was reduced from 533 to 120, which explained why InGaN mode lasing was greatly suppressed in the truncated-rods experiment. In the monolithic rod lattice, the photons leaking out of one rod would be reharvested by adjacent ones. Under a small excitation area, InGaN modes were still unprivileged because photons were likely to be reabsorbed by surrounding unexcited rods. Therefore, the Q -factor of InGaN mode would be lower than that of GaN modes due to the stronger negative feedback from surrounding unexcited rods. As the excitation area increased, the positive feedback among the large number of excited rods enhanced the Q -factor of InGaN modes much more significantly, resulting in the mode-switching phenomena in Figures 4 and 5.

Further, the interaction of vicinal WGM modes introduced new eigenmodes, or supermodes, with shifted resonant wavelengths (λ_s) from the original one (λ_o). To investigate

the mode profile and wavelength shift of these supermodes, mode simulation was reduced from three-dimensional to two-dimensional without loss of generality. Figure 7b,c shows supermodes existing in a hexagon dimer with a 50 nm rod-to-rod spacing with the opposite parities. Figure 7d,e shows another two supermodes with more rods under a higher symmetry. In general, forming optical “bonds” resulted in wavelength redshift ($\Delta\lambda = \lambda_s - \lambda_o > 0$) while forming “nodes” caused blueshift ($\Delta\lambda = \lambda_s - \lambda_o < 0$). The amount of wavelength shifts ranged from few angstroms to one nanometer, which was consistent with the mode spacing in experiment data.

In conclusion, we demonstrated a monolithic GaN/InGaN core-shell nanorod lattice lasing under room temperature. This pattern-and-regrowth processing is capable of fabricating closely coupled high Q cavities with strictly defined geometry in large area. With widely tunable active materials bandgap and precisely controllable lattice geometries, this design is versatile in broad spectral region after a careful redesign in cavity geometry and processing condition optimization. The collective lasing behavior and existence of supermodes revealed the strong interaction among adjacent rods. Therefore, this design is also potential for on-chip coupled resonators waveguides,^{24–27} providing new building blocks for future on-chip light manipulation in visible and ultraviolet spectral range.

■ ASSOCIATED CONTENT

Supporting Information

The Supporting Information is available free of charge on the ACS Publications website at DOI: 10.1021/acs.nanolett.7b02922.

Detailed processing procedures for the tip-passivated nanorod array accompanied by figure illustrations and In composition profile analysis by energy dispersion spectroscopy (PDF)

■ AUTHOR INFORMATION

Corresponding Author

*E-mail: yenhuang@nctu.edu.tw.

ORCID

Chia-Yen Huang: 0000-0003-0844-1903

Notes

The authors declare no competing financial interest.

■ ACKNOWLEDGMENTS

The authors would like to acknowledge Dr. Yu-Hsun Chou and Yu-Hao Hsiao for their assistance in PL measurement and Dr. David Lin for the contribution in the early processing development. This study was supported financially by the Ministry of Science and Technology, Taiwan, under contract no. MOST 106-2221-E-009-119.

■ REFERENCES

- (1) Nakamura, S.; Pearson, S.; Fasol, G. *The Blue Laser Diode: The Complete Story*; Springer: Berlin, 2000.
- (2) Lu, T. C.; Lu, et al.; Chen, S. W.; Wu, T. T.; Tu, M. P.; Chen, C. K.; Chen, C. H.; Li, Z. Y.; Kuo, H. C.; Wang, S. C. *Appl. Phys. Lett.* **2010**, *97*, 071114.
- (3) Kelchner, K. M.; Farrell, R. M.; Lin, Y. D.; Hsu, P. S.; Hardy, M. T.; Wu, F.; Cohen, D. A.; Ohta, H.; Speck, J. S.; Nakamura, S.; et al. *Appl. Phys. Express* **2010**, *3*, 092103.

- (4) Sun, Y.; Zhuo, K.; Sun, Q.; Liu, J. P.; Feng, M. X.; Li, Z. C.; Zhou, Y.; Zhang, L. Q.; Li, D. Y.; Zhang, S. M.; Ikeda, M.; Liu, S.; Yang, H. *Nat. Photonics* **2016**, *10*, 595–600.
- (5) Johnson, J. C.; Choi, H. J.; Knutsen, K. P.; Schaller, R. D.; Yang, P. D.; Saykally, R. J. *Nat. Mater.* **2002**, *1*, 106–110.
- (6) Qian, F.; Li, Y.; Gradečak, S.; Park, H. G.; Dong, Y.; Ding, Y.; Wang, Z. L.; Lieber, C. M. *Nat. Mater.* **2008**, *7*, 701–706.
- (7) Gradečak, S.; Qian, F.; Li, Y.; Park, H. G.; Lieber, C. M. *Appl. Phys. Lett.* **2005**, *87*, 173111.
- (8) Li, C.; Wright, J. B.; Liu, S.; Lu, P.; Figiel, J. J.; Leung, B.; Chow, W. W.; Brener, I.; Koleske, D. D.; Luk, T. S.; Feezell, D. F.; Brueck, S. R. J.; Wang, G. T. *Nano Lett.* **2017**, *17*, 1049–1055.
- (9) Tamboli, A. C.; Haberer, E. D.; Sharma, R.; Lee, K. H.; Nakamura, S.; Hu, E. L. *Nat. Photonics* **2007**, *1*, 61–64.
- (10) Aharonovich, I.; Niu, N.; Rol, F.; Russell, K. J.; Woolf, A.; El-Ella, H. A. R.; Kappers, M. J.; Oliver, R. A.; Hu, E. L. *Appl. Phys. Lett.* **2011**, *99*, 111111.
- (11) Sellés, J.; Brimont, C.; Cassabois, G.; Valvin, P.; Guillet, T.; Roland, I.; Zeng, Y.; Checoury, X.; Boucaud, P.; Mexis, M.; Semond, F.; Gayral, B. *Sci. Rep.* **2016**, *6*, 1–7.
- (12) You, S.; Detchprohm, T.; Zhu, M.; Hou, W.; Preble, E. A.; Hanser, D.; Paskova, T.; Wetzel, C. *Appl. Phys. Express* **2010**, *3*, 102103.
- (13) Brinkley, S. E.; Lin, Y. D.; Chakraborty, A.; Pfaff, N.; Cohen, D.; Speck, J. S.; Nakamura, S.; DenBaars, S. P. *Appl. Phys. Lett.* **2011**, *98*, 011110.
- (14) Koester, R.; Hwang, J. S.; Salomon, D.; Chen, X.; Bougerol, C.; Barnes, J. P.; Dang, D. L. S.; Rigutti, L.; Bugallo, A. L.; Jacopin, G.; Tchernycheva, M.; Durand, C.; Eymery, J. *Nano Lett.* **2011**, *11*, 4839–4845.
- (15) Chang, J. R.; Chang, S. P.; Li, Y. J.; Cheng, Y. J.; Sou, K. P.; Huang, J. K.; Kuo, H. C.; Chang, C. Y. *Appl. Phys. Lett.* **2012**, *100*, 261103.
- (16) Chang, S. P.; Sou, K. P.; Chen, C. H.; Cheng, Y. J.; Huang, J. K.; Lin, C. H.; Kuo, H. C.; Chang, C. Y.; Hsieh, W. F. *Opt. Express* **2012**, *20*, 12457–12462.
- (17) Nobis, T.; Kaidashev, E. M.; Rahm, A.; Lorenz, M.; Grundmann, M. *Phys. Rev. Lett.* **2004**, *93*, 103903.
- (18) Nakagawa, A.; Ishii, S.; Baba, T. *Appl. Phys. Lett.* **2005**, *86*, 041112.
- (19) Atlasov, K. A.; Rudra, A.; Dwir, B.; Kapon, E. *Opt. Express* **2011**, *19*, 2619–2625.
- (20) Hodaie, H.; Miri, M. A.; Heinrich, M.; Christodoulides, D. N.; Khajavikhan, M. *Science* **2014**, *346* (2014), 975–978.
- (21) Jackson, J. *Classical Electrodynamics*; 3rd ed. John Wiley & Sons: New York, 1999.
- (22) Yu, G.; Wang, G.; Ishikawa, H.; Umeno, M.; Soga, T.; Egawa, T.; Watanabe, J.; Jimbo, T. *Appl. Phys. Lett.* **1997**, *70*, 3209.
- (23) Laws, G. M.; Larkins, E. C.; Harrison, I.; Molloy, C.; Somerford, D. J. *Appl. Phys.* **2001**, *89*, 1108.
- (24) Yariv, A.; Xu, Y.; Lee, R. K.; Scherer, A. *Opt. Lett.* **1999**, *24*, 711–713.
- (25) Olivier, S.; Smith, C.; Rattoer, M.; Benisty, H.; Weisbuch, C.; Krauss, T.; Houdré, R.; Oesterlé, U. *Opt. Lett.* **2001**, *26*, 1019–1021.
- (26) Poon, J. K.; Zhu, L.; DeRose, G. A.; Yariv, A. *Opt. Lett.* **2006**, *31*, 456–458.
- (27) Notomi, M.; Kuramochi, E.; Tanabe, T. *Nat. Photonics* **2008**, *2*, 741–747.